A Journal of the Gesellschaft Deutscher Chemiker

Angewandte International Edition GDCh Chemie

www.angewandte.org

Accepted Article

Title: Ultrafast Synthesis of Nanoscale Metal Borides for Efficient Hydrogen Evolution

Authors: Tingting Liu, Chen Chen, Zonghua Pu, Qiufeng Huang, Jiadong Jiang, Min Han, Wei Chen, Guangtao Yu, Yuzhi Sun, Shengyun Huang, Qingjun Chen, Abdullah M. Al-Enizi, Ayman Nafady, Xueqin Mu, and Shichun Mu

To be cited as: *Angew. Chem. Int. Ed.* **2025**, e202425257

Link to VoR: https://doi.org/10.1002/anie.202425257

WILEY VCH

RESEARCH ARTICLE

WILEY VCH

Ultrafast Synthesis of Nanoscale Metal Borides for Efficient Hydrogen Evolution

Tingting Liu,[a] Chen Chen,[a] Zonghua Pu,*[a] Qiufeng Huang,*[a] Jiadong Jiang,[b] Min Han,*[b] Wei Chen,[a] Guangtao Yu,[a] Yuzhi Sun,[c] Shengyun Huang,[c] Qingjun Chen,*[c] Abdullah M. Al-Enizi,[d] Ayman Nafady,[d] Xueqin Mu,[e] Shichun Mu*[e]

[a] Dr. T. Liu, C. Chen, Prof. Z. Pu, Prof. Q. Huang, Prof. W. Chen, Prof. G. Yu
Fujian Key Laboratory of Polymer Materials, College of Chemistry and Materials Science, Fujian Normal University, Fuzhou, Fujian, 350117, P. R. China
E-mail: zonghua.pu@fjnu.edu.cn; qiufenghuang@fjnu.edu.cn

[b] J. Jiang, Prof. M. Han
Fujian Cross Strait Institute of Flexible Electronics (Future Technology), Fujian Normal University, Fuzhou, Fujian, 350117, P. R. China
E-mail: 07203@njnu.edu.cn

[c] Y. Sun, Dr. S. Huang, Prof. Q. Chen
Ganjiang Innovation Academy, Key Laboratory of Rare Earths, Chinese Academy of Sciences, Ganzhou 341000, P. R. China
E-mail: qjchen@gia.cas.cn

[d] Prof. A. Al-Enizi, Prof. A. Nafady
Department of Chemistry, College of Science, King Saud University, Riyadh 11451, Saudi Arabia

[e] X. Mu, Prof. S. Mu,
State Key Laboratory of Advanced Technology for Materials Synthesis and Processing, Wuhan University of Technology, Wuhan 430070, P. R. China
E-mail: msc@whut.edu.cn

Abstract: Nanoscale metal borides, with exceptional physicochemical properties, have been attracted widespread attention. However, traditional synthesis methods of metal borides often lead to surface coking and large particle sizes. Herein, we have employed a flash Joule heating (FJH) technique to enable the ultrafast synthesis of metal boride nanomaterials. The synthesized materials encompass a wide range of diverse categories, including alkaline-earth metal borides (CaB_6), transition metal borides (TiB_2, VB_2, CrB_2, MoB, MoB_2, MnB_2, MnB_4, FeB, CoB, NiB), noble-metal borides (RuB_2, $RuB_{1.1}$), and rare-earth metal borides (LaB_6, CeB_6). As an example, the RuB_2 demonstrates highly desirable electrocatalytic performance for all-pH hydrogen evolution reaction (HER). Especially, under the acidic condition, it exhibits an overpotential as low as 15 mV at a current density of 10 mA cm^{-2}, with a nearly 100% faradic efficiency. Additionally, in situ Raman spectra confirm that both Ru and B sites serve as active sites for the HER. Moreover, the stability of RuB_2 can be further enhanced by optimizing the microenvironments of the anolyte composition (H^+, K^+). More importantly, the experimental and density functional theory (DFT) calculations reveal that the co-existence of H^+ and K^+ localized around the RuB_2 plays a crucial role in further enhancing the stability.

Introduction

The metal (M)-boron (B) alloys consisting of M-M metallic bonds, M-B ionic bonds and B-B covalent bonds, confer upon them a diverse range of properties, including extreme hardness, high temperature resistance, oxidation resistance, remarkable thermal stability, good thermal conductivity, and outstanding chemical durability.[1-3] Additionally, certain borides also have high electrical conductivity, rendering them with tremendous potential for various applications.[4,5] For instance, the utilization of nanostructured metal borides (MBs) has garnered significant attention in various fields such as ultra-hard and ultra-strong ceramics, and catalyst supports, owing to their robust metal-substrate interactions and distinctive electronic structures that make them are promising candidates for catalysts.[5,6] Nevertheless, the conventional methods for the synthesizing borides with good crystallinity and stability necessitate high temperature and/or high pressure, resulting in coked surfaces and large particle sizes for MBs, which are detrimental to their catalytic performance.[7,8]

Much effort has been devoted to synthesizing MBs with fine particle sizes, including the chemical reduction, molten salt assistance, metallothermic reduction, and hydro/solvothermal methods. The chemical reduction method involves the direct reduction of metal salt using sodium borohydride ($NaBH_4$) under ambient temperature. By employing this approach, a range of amorphous MBs including Fe-B, Co-B, Ni-B, Cu-B, and Pd-B can be synthesized.[9-12] Despite the potential benefits of nanoscale materials with increased surface area and enhanced catalytic activity for these amorphous MBs, their crystallinity is typically compromised, leading to diminished stability. The halide molten salt-assisted method at high temperatures is an effective strategy to prepare MBs (M= W, Hf, Ta, Mn, Ti, Mo, Zr, V, Cr, etc.) with nanoscale structures and good crystallinity. Nevertheless, its notable drawback lies in the low eutectic point (> 776 ℃) and volatility of the halide molten salt during heat treatment, which poses challenges as the synthesis temperature for MBs typically exceeds 800 ℃.[13-16] On the other hand, the metal salt exhibits significant corrosiveness and volatility when exposed to high temperatures. The metallothermic reduction reaction method, employing strong reductant such as Al, Sn, Mg, Na, K,

represents an alternative approach for synthesis of MBs.[17-19] Its primary limitation stems from the heightened reactivity exhibited by strong reducing metals (Na, K, etc.), which causes significant safety risks during the reaction. Additionally, strong acids are required to remove any excess metal reducing agents after the reaction.[20] Although some of the MBs can be obtained by facile methods, the type of MBs is also very limited. Therefore, the development of facile, versatile, and scalable methods for synthesis of MBs with nanoscale structures and good crystallinity is highly desired but remains a formidable challenge.

The technique of flash Joule heating (FJH) involves the application of a millisecond current pulse to the precursor, rapidly elevating the sample temperature to ultrahigh levels (>3000 K), followed by swift cooling to room temperature at a rate exceeding 10^4 K s^{-1}. The rapid and instantaneous fluctuation of temperatures can lead to the completion of the reaction within a few seconds. Additionally, the second-level calcination time simultaneously prevents the occurrence of sintering and agglomeration of active components resulting from prolonged heat treatment, ensuring rapid and effective dispersion of active atoms. This potentially facilitates precise structural regulation of the synthesized material.[21] For example, Hu's group pioneered the application of the FJH method for synthesis of a series of high-entropy alloys, featured by nanoparticles with an average size of approximately 5 nm. Recently, the FJH method has also been employed by Tour's group to fabricate a series of metal dichalcogenides.[22]

In this work, by means of FJH, fifteen significant MBs, including alkaline-earth metal borides (CaB_6), transition metal borides (TiB_2, VB_2, CrB_2, MoB, MoB_2, MnB_2, MnB_4, FeB, CoB, NiB), noble-metal borides (RuB_2, $RuB_{1.1}$), and rare-earth-based metal borides (LaB_6, CeB_6) are synthesized. As an exemplary case, the hydrogen evolution reaction (HER) electrocatalytic performance of RuB_2 has been investigated, revealing exceptional activity and stability. Experimental investigations further demonstrate that the outstanding catalytic performance of RuB_2 towards the HER, achieved by FJH, can be attributed to its small nanoparticle size, significant exposure of electrochemical surface area, and rapid kinetics of charge transfer. Additionally, the catalytic stability of RuB_2 can be significantly enhanced by optimizing the microenvironments of the anolyte composition, specifically through careful adjustment of H^+ and K^+ concentrations. More significantly, the coexistence of localized H^+ and K^+ ions around RuB_2 is found to play a pivotal role in further augmenting its stability, as revealed by experimental investigations and density functional theory (DFT) calculations.

Results and Discussion

The typical synthesis mechanism is illustrated in **Figure 1a**. First, the metal salts or oxides combined with a precise quantity of $NaBH_4$ were used as precursors. Subsequently, the above precursor mixture was subjected to FJH under Ar flow. After the mixture was cooled down, the byproduct (BO_x, Na^+, etc.) was thoroughly rinsed with deionized water, and then the product was obtained. It is worth noting that the FJH process can achieve ultrahigh temperatures (~3000 K), which enables the fabrication of over fourteen MBs (**Figure 1b).**

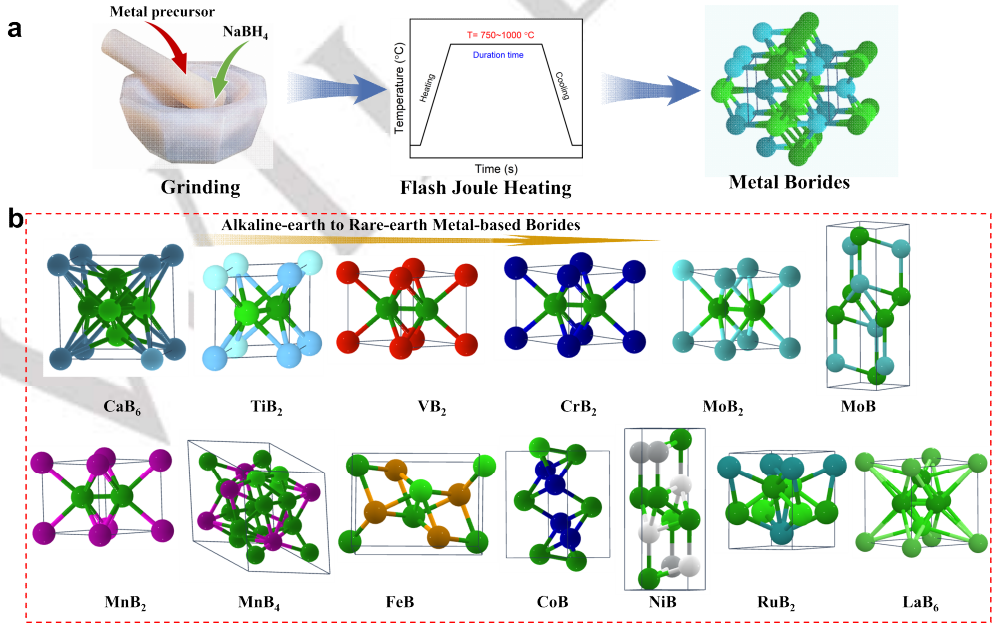

Figure 1. (a) Schematic diagram of the preparation of metal borides by FJH. Green and blue balls denote boron and metal elements. (b) The crystal structures of thirteen metal borides from alkaline earth to rare-earth.

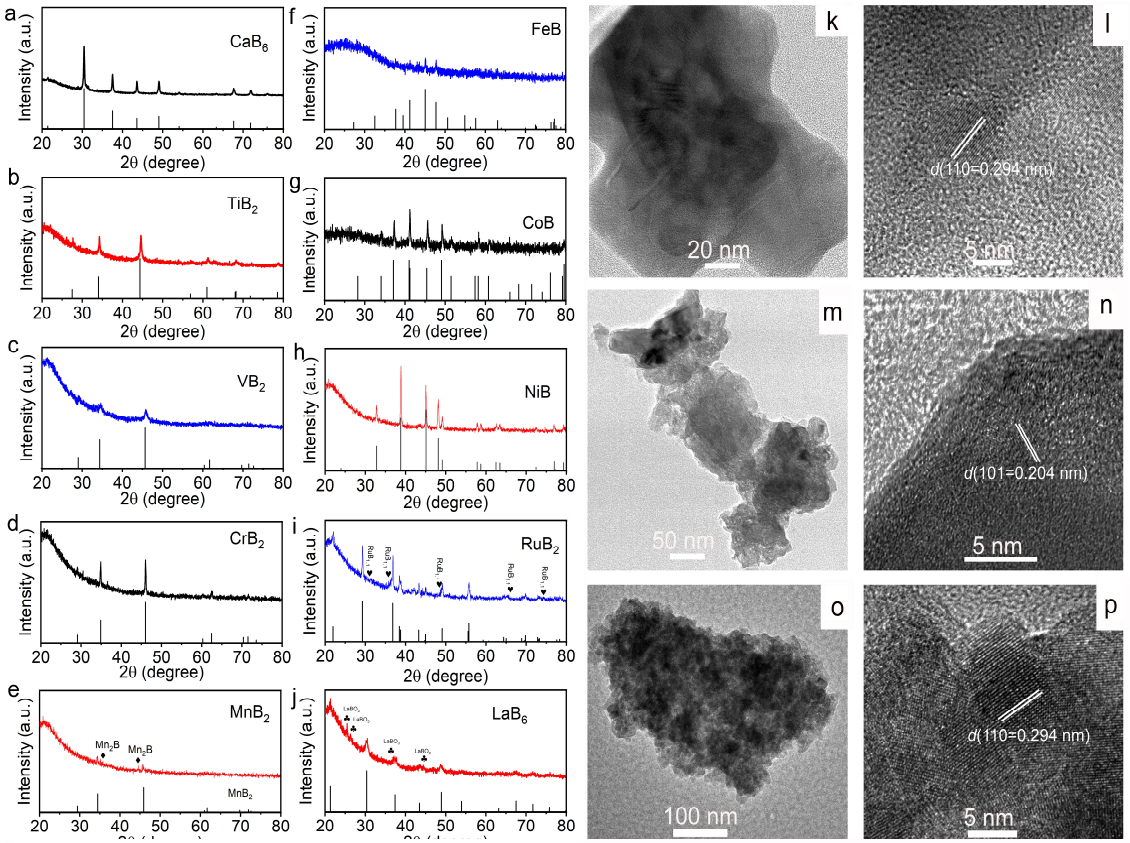

Figure 2. (a-j) The crystal structures of ten borides. The XRD patterns for (a) CaB_6, (b) TiB_2, (c) VB_2, (d) CrB_2, (e) MnB_2, (f) FeB, (g) CoB, (h) NiB, (i) RuB_2, (j) LaB_6. (k, m, o) TEM and (l, n, p) HRTEM images of (k, l) CaB_6, (m, n) TiB_2, (o, p) LaB_6.

The typical metal precursors commonly used and the parameters of FJH are presented in **Table S1**. To ensure the complete conversion of metal precursors into metal borides, a slight excess of $NaBH_4$ has been employed in experimental studies relative to the molar ratio of metal to boron (**Table S1**). The unreacted precursor and by-products can be effectively eliminated through multiple washes with deionized water. Additionally, the utilization of halides or oxides as the optimal metal precursor is considered for several reasons: First, due to the hydrolysis of $NaBH_4$ in aqueous solutions, precursors devoid of crystal water are preferable. Second, the pyrolysis process of $NaBH_4$ leads to the generation of H_2, B, and NaH ($NaBH_4 \rightarrow NaH + B + 3/2H_2$). Thus, considering potential safety concerns associated with the release of O_2 by pyrolysis of metal nitrites, it is imperative to avoid utilization of nitrites. Consequently, employing metal halides or oxides emerges as the optimal approach for synthesis of metal borides. Due to the ultrahigh operating temperature by the FJH process, a range of MBs spanning from alkaline earth to rare-earth elements, such as CaB_6, TiB_2, VB_2, CrB_2, MnB_2, FeB, CoB, NiB, RuB_2, and LaB_6 were readily synthesized using various of low-cost metal precursors (**Figures 2a-j**). Undoubtedly, this further demonstrates that FJH is a versatile and cost-effective method for synthesizing MBs. As illustrated in **Figures 2a-j,** the powder X-ray diffraction (XRD) patterns of CaB_6, TiB_2, VB_2, CrB_2, FeB, CoB and NiB are match well with their standard PDF cards.[23-25] However, the XRD patterns of MnB_2, RuB_2, and LaB_6 shows a small amount of impurity of Mn_2B, $RuB_{1.1}$, and $LaBO_3$, respectively. It is worth noting that for iron-group metal (Fe, Co, Ni), it is feasible to readily obtain FeB, CoB, and NiB phases even with excessive usage of $NaBH_4$. Conversely, for alkaline earth or rare earth metal, achieving a metal-to-B ratio of 1:6 can be easily accomplished (**Figure S1**).[23,26] The morphologies of these borides are revealed by scanning electron microscopy (SEM) and transmission electron microscopy (TEM) (**Figure 2k-p**, **Figures S2** and **S3**). NiB, CoB, MnB_2 and CrB_2 are composed of nanoparticles, FeB shows a nanoflower morphology, and other MB samples (CaB_6, LaB_6, VB_2, TiB_2,) possess a typical nanosheet structure. Furthermore, typical MBs of alkaline earth metal borides (CaB_6), transition metal borides (TiB_2, VB_2, CrB_2) and rare-earth-based metal borides (LaB_6) were characterized by high-magnification TEM, which indicate that CaB_6, TiB_2, and LaB_6 possess a typical nanosheet structure (**Figure 2k, 2m, 2o, and 3a-c**), while VB_2 and CrB_2 consists of small nanoparticles **(Figure S3c and d**). Additionally, the high-resolution TEM (HRTEM) image shows the lattice fringe spacing of CaB_6, TiB_2, LaB_6 is 0.294, 0.204 and 0.294 nm, corresponding to the cubic CaB_6 (110), hexagonal TiB_2 (101) and cubic LaB_6 (110) crystal planes (**Figures 2l, 2n, 2p**), respectively. Furthermore, several metal borides including MnB_4, $RuB_{1.1}$, VB (with a small amount of V_2O_3), CeB_6, MoB, and α-MoB_2 can be successful prepared by controlling the precursors relative to the metal-to-boron ratio

(**Figures S4** and **S5**). It is worth noting that, despite the quality of some obtained materials still requires improvement, our work offers a robust method for the synthesis and subsequent investigation of the properties and potential applications of borides. Consequently, it is anticipated that this Joule heating technique could pave the way for the development of a wide range of advanced boride-based functional materials.

Generally, materials based on VIIIB group metal (such as Fe, Co, Ni, etc.) possess good HER activity. Therefore, the HER activity of FeB, CoB, NiB, $RuB_{1.1}$ and RuB_2 was further investigated. As illustrated in **Figure S6**, these compounds exhibited overpotentials of 509 mV for CoB, 412 mV for FeB, 170 mV for NiB, 54 mV for $RuB_{1.1}$ and 15 mV for RuB_2 at a current density of 10 mA cm^{-2} in 0.5 M H_2SO_4 solutions, respectively. Notably, RuB_2 displays the highest HER activity among them. Consequently, we conducted a detailed investigation on RuB_2 as a typical example.

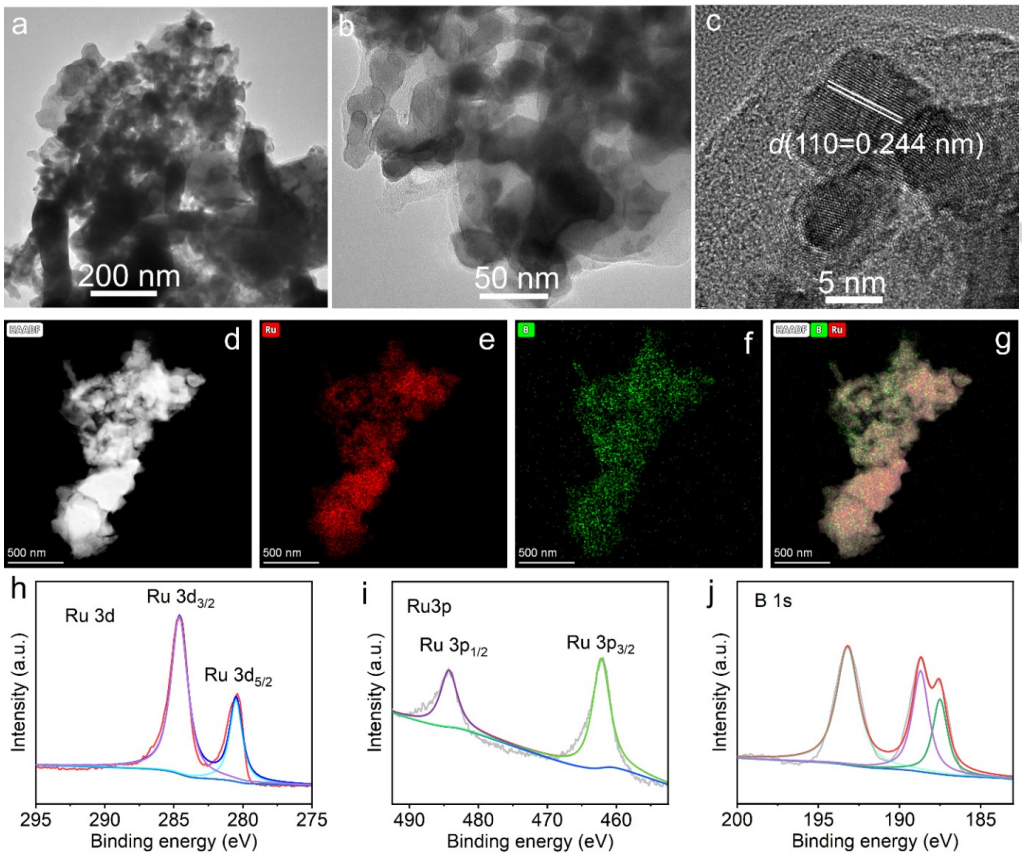

Figure 3. (a and b) TEM, (c) HRTEM, and (d-g) HAADF images and EDX elemental mapping of Ru, and B, of FJH RuB_2. XPS spectra in the (h) Ru 3d, (i) Ru 3p and (j) B 1s regions for FJH RuB_2.

Next, the morphology and surface component of RuB_2 sample was further characterized by high-angle annular dark-field scanning transmission electron microscopy (HAADF-STEM) and X-ray photoelectron spectroscopy (XPS). The TEM images in **Figures 3a-b** reveal the presence of numerous nanoparticles within RuB_2, with a particle diameter range from 5 to 200 nm (**Figure S7**). The small nanoparticle size of RuB_2 obtained can be attributed to the methodology employed by FJH, which effectively avoids sintering and agglomeration of active components caused by prolonged heat treatment during second-level calcination. This ensures rapid and effective dispersion of active atoms, while also regulating the micro-morphology, composition, and structure of synthetic materials. In stark contrast, direct pyrolysis of $RuCl_3$ and $NaBH_4$ resulted in the formation of bulk RuB_2 particles with diameters large than 100 nm (**Figures S8a-f**). Additionally, the HRTEM image in **Figure 3c** exhibits a well-defined lattice fringe spacing of 0.244 nm, which closely corresponds to the observed diffraction pattern associated with the (110) crystal plane of orthorhombic phase RuB_2.[27] The energy dispersive spectroscopy (EDS) analysis reveals the presence of both Ru and B signals in the RuB_2 nanoparticles (**Figure S9**). Moreover, HAADF-STEM and EDS elemental mapping images reveal the homogeneous distribution of both Ru and B elements within the RuB_2 nanoparticle (**Figures 3d-g**). Ru 3d, Ru 3p and B 1s XPS spectra are presented in **Figure 3h-j**. Regarding the Ru 3d spectrum, the peaks observed at binding energies (BE) of 280.4 and 284.6 eV correspond to the Ru $3d_{5/2}$ and Ru $3d_{3/2}$ states of RuB_2, respectively. Concerning the Ru 3p spectrum, the peaks detected at energies of 484.3 and 462.2 eV can be attributed to

the Ru $3p_{1/2}$ and Ru $3p_{3/2}$ states, respectively. Additionally, **Figure 3j** illustrates that the B 1s spectrum of RuB_2 has two distinct subpeaks at 187.5 and 188.7 eV, which can be attributed to the Ru-B bond in RuB_2. Furthermore, the peak located at 193.2 eV is assigned to metaborate/borate species (BO_x) resulting from surface oxidation of RuB_2 when exposed to air.[28] All of these observations demonstrate that the RuB_2 nanoparticles were successfully obtained.

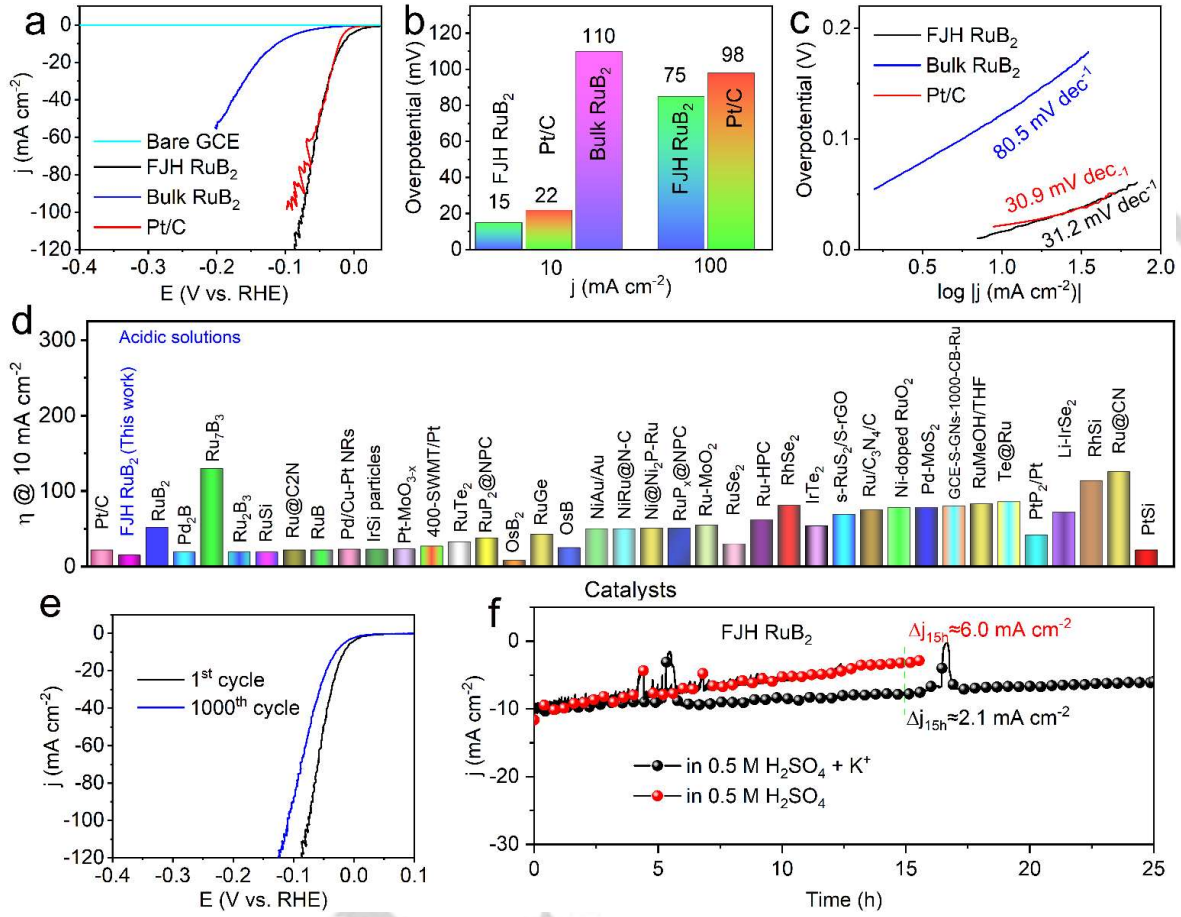

Figure 4. HER performances of different catalysts in 0.5 M H_2SO_4 solutions. (a) Polarization curves of bare GCE, FJH RuB_2, bulk RuB_2, and Pt/C. (b) Overpotentials at j = 10 and 100 mA cm^{-2} for FJH RuB_2, RuB_2, and Pt/C. (c) Tafel plots derived from polarization curves. (d) Comparison of the overpotentials at 10 mA cm^{-2} with recently reported HER catalysts under acidic medium. (e) Polarization curves were recorded before and after 1000 cycles for FJH RuB_2. (f) i-t curve for FJH RuB_2 at j = 10 mA cm^{-2} in 0.5 M H_2SO_4 (red curve) and 0.5 M H_2SO_4 + K^+ (without iR correction).

The HER performance of RuB_2 prepared by FJH (FJH RuB_2) was evaluated in a H_2-saturated 0.5 M H_2SO_4 solution using a conventional three electrode system. Additionally, bare glassy carbon electrode (GCE), commercially available 20 wt% Pt/C material (Johnson Matthey) and bulk RuB_2 were employed as benchmark. The potentials were calibrated against the reverse hydrogen electrode (RHE) as shown in **Figure S10** for standardization purposes. Prior to conducting the HER tests, the RuB_2 catalyst was subjected to activation through multiple cycles of linear sweep voltammetry (LSV) within the voltage window applied for the HER. All polarization curves were recorded with *iR* compensation, and the internal resistance was determined using electrochemical impedance spectroscopy (EIS) (**Figure S11**). The bare GCE shows the negligible HER activity, as displayed in **Figure 4a,** whereas the overpotential (η) versus RHE at a geometric current density of 10 mA cm^{-2} for FJH RuB_2, Pt/C and bulk RuB_2 catalysts are 15, 22 and 110 mV, respectively (**Figure 4b**). This demonstrates FJH RuB_2 has higher HER activity than bulk RuB_2 and Pt/C. It is worth mentioning that FJH RuB_2 (75 mV) even exhibits 23 mV lower overpotential than commercial Pt/C (98 mV) at a larger current density of 100 mA cm^{-2}, further indicating the superior HER activity of RuB_2 over Pt/C under high current density conditions. More importantly, the catalytic activity of FJH RuB_2 surpasses that of recently reported RuB_2-based catalysts, including phase-pure RuB_2 (52 mV@ 10 mA cm^{-2}),[29] RuB_2 obtained by solid-state metathesis (18 mV@ 10 mA cm^{-2}),[27] and RuB_2 synthesized by metallothermic reduction (15.6 mV@ 10 mA cm^{-2}).[20] The high HER activity can be attributed to its small

nanoparticle size (5-200 nm) by FJH, whereas larger particle sizes ranging from 11 to 300 nm have to be obtained by traditional synthesis methods.[20,27,29] The Tafel slope of Pt/C (30.9 mV dec^{-1}) is consistent with the reported value[30] (**Figure 4c**). Moreover, FJH RuB_2 exhibits a slightly lower Tafel slope (31.2 mV dec^{-1}) compared to bulk RuB_2 (80.5 mV dec^{-1}), suggesting that the kinetics of the HER are influenced by particle size. Furthermore, to the best of our knowledge, FJH RuB_2 exhibits superior HER activity compared to most other noble-metal-based HER catalysts in acidic aqueous solutions (**Figure 4d** and **Table S2**).

Subsequently, the stability of FJH RuB_2 was evaluated by cyclic voltammetry (CV) at an accelerated scan rate of 100 mV s^{-1}. The LSV measurements were performed periodically after 1000 CV cycles, as depicted in **Figure 4e**. It can be observed that the polarization curve of FJH RuB_2 shows a slight degradation following 1000 CV cycles. Specifically, to achieve a current density of 100 mA cm^{-2}, the LSV of FJH RuB_2 experiences a negative shift of ~ 30 mV after 1000 CV cycles. In addition, long-term chronoamperometry at the overpotential of ~20 mV was tested to further monitor the stability of FJH RuB_2 in 0.5 M H_2SO_4 electrolyte. FJH RuB_2 exhibits moderate stability ($\Delta j \approx 6.0$ mA cm^{-2}) over a period of 15 h, as depicted in **Figure 4f** (red curve). It is worth noted that the stability of RuB_2 can be further enhanced ($\Delta j \approx 2.1$ mA cm^{-2} over a period of 15 h electrolysis) by optimizing the microenvironments of the electrolyte through introduction of microelement K^+ (**Figure 4f** black curve), while maintaining its original HER activity (**Figure S12**). Meanwhile, with the introduction of K^+, there is no significant change observed in the pH values of 0.5 M H_2SO_4 (**Figure S13**). After the stability test, XRD characterization was utilized to probe the FJH RuB_2 catalyst. As shown in **Figure S14**, the XRD pattern exhibits a strong resemblance between the FJH RuB_2 and its standard PDF card, indicating exceptional catalytic stability towards the HER in 0.5 M H_2SO_4 electrolyte. It is noteworthy that the HER activity of FJH RuB_2 was further investigated under neutral and alkaline media. As illustrated in **Figure S15**, FJH RuB_2 also exhibits outstanding HER activity under 1.0 M KOH and 1.0 M phosphate buffer solution (PBS), requiring overpotentials of 9 and 37 mV, respectively, to achieve a current density of 10 mA cm^{-2}. Moreover, FJH RuB_2 demonstrates enhanced stability for the HER in alkaline conditions compared to neutral or acidic environments (**Figure S16**). All of these analysis results indicate the excellent catalytic activity and good stability of FJH RuB_2 towards HER.

The faradaic yields for H_2 production from the FJH RuB_2 materials was determined by subjecting catalyst-loaded carbon paper working electrodes (with approximately 0.34 mg RuB_2 loaded on 0.5 cm×0.5 cm carbon paper) to a constant cathodic current of around 19 mA for a duration of 4031 s, leading to the transfer of a total charge amounting to 76.28 coulombs. The H_2 gas generated during the experiment was effectively collected using a water drainage technique as illustrated in **Figure S17**.[31,32] Notably, clear observation of the produced gas can be made on the surface of carbon paper supporting FJH RuB_2 catalysts (**Figure S18**). Additionally, **Video S1** provides visual evidence showcasing the dynamic process of both water splitting and hydrogen accumulation. It is noteworthy that experimental measurements reveal a close agreement between the evolved hydrogen quantity and its theoretical prediction based on Faraday's law, thus confirming ~ 100% Faradaic yields for FJH RuB_2 as depicted in **Figures S19** and **S20**. Collectively, these findings unequivocally establish FJH RuB_2 as an exceptional and enduring catalyst for overall water electrolysis under acidic conditions.

To gain a comprehensive understanding of the exceptional catalytic activity exhibited by FJH RuB_2, we investigated the electrochemical active surface area (ECSA) of both FJH RuB_2 and bulk RuB_2 using a conventional CV method (**Figure S21**).[33] The double-layer capacitance (C_{dl}) values of FJH RuB_2 and bulk RuB_2 were measured as 1.52 and 0.345 mF cm^{-2} (**Figure S22**), respectively. Thus, the presence of a larger ECSA of FJH RuB_2 compared to bulk RuB_2 implies an increased number of exposed catalytic active sites, which are well-suited for enhancing the performance of FJH RuB_2 during the HER catalytic process.[34,35] In addition, the Nyquist plots illustrate that the charge-transfer resistance (R_{ct}) of the FJH RuB_2 is lower than that of bulk RuB_2 (**Figure S23**), indicating a heightened capacity for charge-transfer during the HER process for FJH RuB_2. Therefore, by harnessing the advantages of FJH RuB_2, including small nanoparticle size, extensive electrochemical surface area exposure, and rapid charge transfer kinetics achieved through FJH, remarkable HER performance is exhibited.

Additionally, in situ Raman spectra were acquired to analyze intermediates of FJH RuB_2 during the HER process. For comparison purposes, commercial RuO_2 was also examined. **Figures 5a** and **b** depict the in-situ Raman spectra of FJH RuB_2 and RuO_2·catalysts at various potentials relative to the RHE. The characteristic Raman peak at 878 cm^{-1} observed in both FJH RuB_2 and RuO_2 is attributed to the stretching vibrations of Ru–H.[36] The Raman peak at ~750 cm^{-1} can be attributed to solvent of water.[37,38]] Additionally, the peaks within the range of 900 to 1100 cm^{-1} can be identified as originating from the H_2SO_4 electrolyte.[39] It is worth noting that the FJH RuB_2 catalyst exhibits the emergence of two distinct Raman peaks at 698 and 1587 cm^{-1} during the HER catalytic process, whereas such peaks are absent in RuO_2. Therefore, these peaks can be attributed to the vibrations of B−H bond during the electrocatalytic process.[40] These results validate the HER catalytic activity of FJH RuB_2, indicating that both Ru and B sites exist as active sites for the HER.

Figures 5c-f further confirm the electron transfer from Ru to B atoms. These surface electron-deficient Ru sites might serve as the active centers for the appropriate adsorption behavior of various reaction intermediates.[41] Moreover, the conduction band of RuB_2 is observed to be crossed by the Fermi level, as evidenced by the projected density of states (PDOS) depicted in **Figure 5g**, indicating a pronounced electron mobility. Moreover, due to a downward shift of the Dirac cone at the G point ensuring rapid electron transfer (**Figure 5h**), RuB_2 exhibits the absence of band gap, which is significant for the electrocatalytic HER.[42] Furthermore, the HER free energy diagram of FJH RuB_2 in different microenvironments (neutral, acid, K^+, co-existence K^+ + H^+) is illustrated in **Figures 5i** and **j**. Specifically, the Gibbs

free energy (ΔG_H^*) of FJH RuB_2 was predicted to be -3.5, -2.3, -1.0 and 0.3 eV in neutral, acid, K^+, co-existence K^+ + H^+ solutions, respectively. The close-to-zero value of ΔG_{H^*} for FJH RuB_2 under the co-existence of K^+ and H^+ suggests an optimized HER catalytic activity in this environment.

Furthermore, the enhanced stability of FJH RuB_2 in the presence of both H^+ and K^+ was investigated through DFT calculations. The typical DFT calculations models of FJH RuB_2 in different solutions is illustrated in **Figure S24-26**. Obviously, as illustrated in **Figure 5k**, the occurrence of charge transfer in different electrolytes is apparent. Typically, in the aqueous phase, H^+ exists predominantly as hydronium ions (H_3O^+). Upon introduction of K^+ into the acidic solution microenvironment, the Bader charge at the catalyst decreases by around 0.89 |e| (**Figure 5l**). It indicates the added cations influencing on the catalyst surface through electric field effect, resulting in a moderate decrease in the migration rate of hydronium ions. Consequently, by modulating the distribution and migration rate of hydronium ions via the electric field effect, it is possible to enhance the stability of the catalyst. The observed trend in the change of electric field distribution is consistent with the previous report.[43-45]

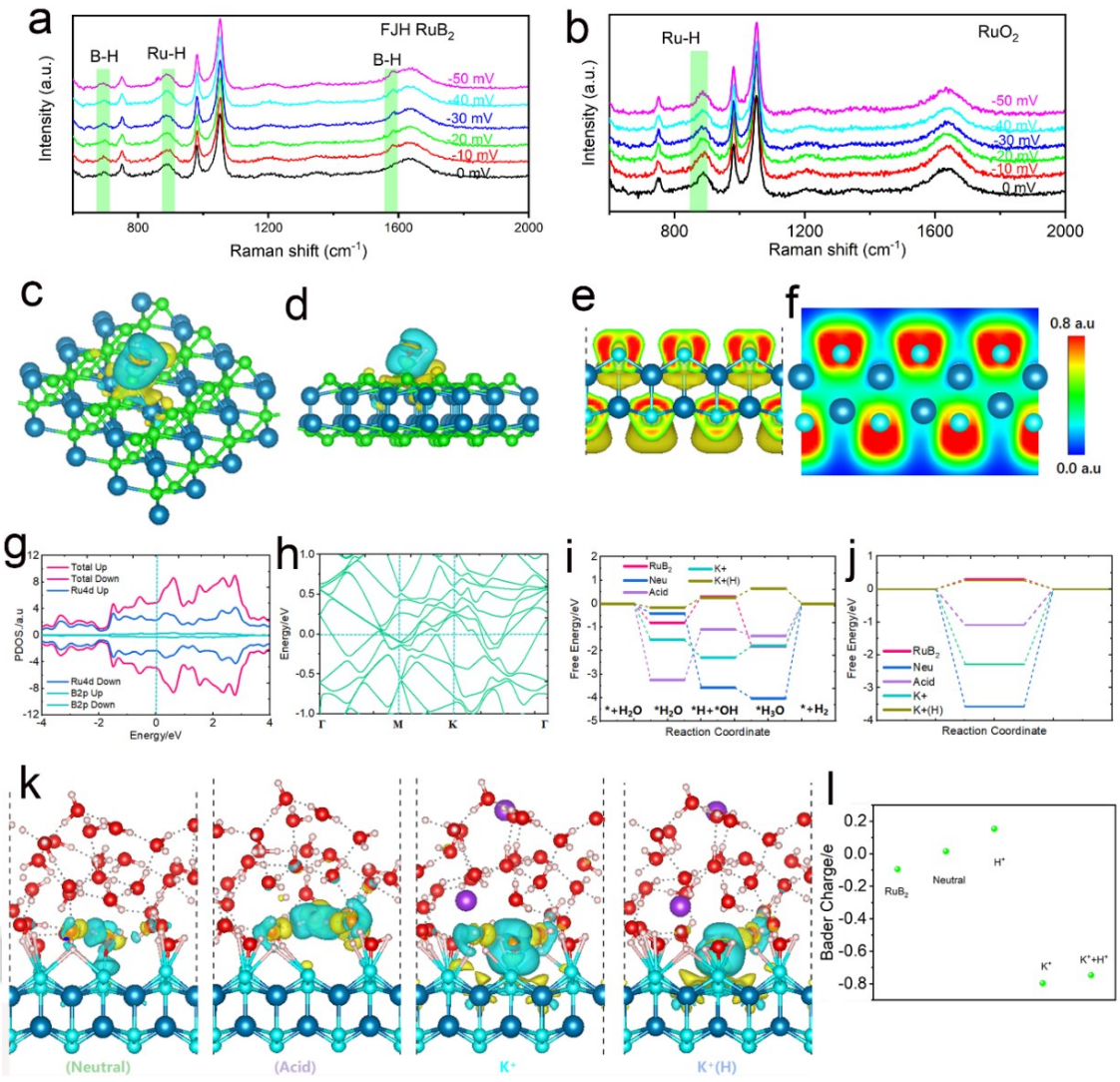

Figure 5. Raman spectra for (a) FJH RuB_2 and (b) RuO_2 in 0.5 M H_2SO_4 solutions. (c and d) The charge density difference at the interface of FJH RuB_2. Yellow and cyan regions represent charge accumulation and depletion, respectively. (e and f) Electron location function (ELF) of RuB_2. (g) PDOS of d, p orbitals of RuB_2. (h) Band structure of RuB_2. (i and j) HER free energy diagram of FJH RuB_2 in different microenvironments. (k) DFT calculation models of the structures of FJH RuB_2 in different electrolyte. (l) The Bader charge (q) of FJH RuB_2 at different conditions.

Conclusion

In summary, the flash Joule heating (FJH) process for metal borides (MBs) synthesis exhibits high energy efficiency compared to traditional furnace heating due to its ultrafast heating/cooling rate, direct sampling heating feature, and the short reaction duration within 60 s. We have successfully demonstrated the synthesis of fifteen significant MBs, encompassing alkaline earth metal borides (CaB_6), transition metal borides (TiB_2, VB_2, CrB_2, MoB, MoB_2, MnB_2, MnB_4, FeB, CoB, NiB), noble-metal-based borides (RuB_2, $RuB_{1.1}$), and rare-earth-based metal borides (LaB_6, CeB_6) through the FJH approach. The electrocatalytic HER performance of RuB_2 has been extensively investigated, demonstrating a remarkable low overpotential of 15 mV at a current density of 10 mA cm^{-2} and exceptional stability in a 0.5 M H_2SO_4 solution, along with 100% faradic efficiency. Such high HER activity is higher than that of the state-of-the-art commercial Pt/C catalyst. Our combined experimental and theoretical investigations further demonstrate that the outstanding catalytic performance of RuB_2 towards HER, achieved by FJH, can be attributed to its small nanoparticle size, substantial exposure of electrochemical surface area, and rapid kinetics of charge transfer. Due to the FJH process, which offers a highly adjustable energy input exceeding 3000 K, coupled with a kinetically controlled ultrafast heating/cooling rate (>10^4 K s^{-1}) is provided. In other words, the FJH process offers a pathway to access numerous non-equilibrium phases and effectively stabilizes them at room temperature. Consequently, it holds great potential as a versatile tool for tailoring the metastable phases of diverse materials including metal carbides/nitrides/borides, high-entropy alloys, single atom, and two-dimensional materials.

Acknowledgements

This work was supported by the National Natural Science Foundation of China (Grant No. 22402030, 62475266), the Fujian Province Young and Middle-Aged Teacher Education Research Project (JZ230009; JZ240012), the Jiangxi Provincial Natural Science Foundation (20232BAB204101), the Youth Innovation Promotion Association of Chinese Academy of Sciences (2023341), A.M.A and Z. Pu extend their sincere appreciation to the Distinguished Scientist Fellowship Program (DSFP) at King Saud University for funding of this work.

Keywords: Metal borides• Joule heating • ultrafast synthesis • electrocatalysis • hydrogen evolution reaction

References

[1] J. Zhou, J. Palisaitis, J. Halim, M. Dahlqvist, Q. Tao, I. Persson, L. Hultman, P. O. Å. Persson, J. Rosen. *Science* **2021**, *373*, 801–805.

[2] K. Kawashima, R. A. Márquez, L. A. Smith, R. R. Vaidyula, O. A. Carrasco-Jaim, Z. Wang, Y. J. Son, C. L. Cao, C. B. Mullins. *Chem. Rev.* **2023**, *123*, 12795–13208.

[3] E. Lee, B. P. T. Fokwa, *Acc. Chem. Res*. **2022**, *55*, 56–64.

[4] Y. Wang, M. Zhang, Z. Kang, L. Shi, Y. Shen, B. Tian, Y. Zou, H. Chen, X. Zou, *Nat. Commun*. **2023**, *14*, 5119.

[5] C. Li, X. Liu, L. Zhu, R. Huang, M. Zhao, L. Xu, Y. Qian, *Chem. Mater*. **2018**, *30*, 6969-6977.

[6] H. Lv, S. Mu, *Nanoscale* **2014**, *6*, 5063.

[7] M. Fan, X. Liang, Q. Li, L. Cui, X. He, X. Zou, *Chin. Chem. Lett*. **2022**, *34*, 107275.

[8] H. Park, A. Encinas, J. P. Scheifers, Y. M. Zhang, B. P. T. Fokwa, *Angew. Chem., Int. Ed*. **2017**, *56*, 5575-5578.

[9] Y. Zhou, F. Che, M. Liu, C. Zou, Z. Liang, P. D. Luna, H. Yuan, J. Li, Z. Wang, H. Xie, H. Li, P. Chen, E. Bladt, R. Quintero-Bermudez, T. Sham, S. Bals, J. Hofkens, D. Sinton, G. Chen, E. H. Sargent, *Nat. Chem*. **2018**, *10*, 974-980.

[10] Y. Jiang, Y. Fang, C. Chen, P. Ni, B. Kong, Z. Song, Y. Lu, L. Niu, *ChemElectroChem* **2019**, *6*, 3684-3689.

[11] J. Li, J. Chen, Q. Wang, W. Cai, S. Chen, *Chem. Mater.* **2017**, *29*, 10060-10067.

[12] Y. Li, B. Huang, Y. Sun, M. Luo, Y. Yang, Y. Qin, L. Wang, C. Li, F. Lv, W. Zhang, S. Guo, *Small* **2019**, *15*, 1804212.

[13] S. K. Gupta, Y. Ma, *Prog. Mater. Sci*. **2021**, *117*, 100734.

[14] J. Zhu, Y. Guo, F. Liu, H. Xu, L. Gong, W. Shi, D. Chen, P. Wang, Y. Yang, C. Zhang, J. Wu, J. Luo, S. Mu, *Angew. Chem., Int. Ed*. **2021**, *133*, 12436-12442.

[15] D. Chen, R. Lu, R. Yu, H. Zhao, D. Wu, Y. Yao, K. Yu, J. Zhu, P. Ji, Z. Pu, Z. Kou, J. Yu, J. Wu, S. Mu, *Nano Micro Lett*. **2023**, *15*, 168.

[16] S. K. Gupta, Y. Mao, *J. Phys. Chem. C* **2021**, *125*, 6508–653.

[17] P. R. Jothi, K. Yubuta, B. P. T. Fokwa, *Adv. Mater*. **2018**, *30*, 1704181.

[18] X. Ai, X. Zou, H. Chen, Y. Su, X. Feng, Q. Li, Y. Liu, Y. Zhang, X. Zou, *Angew. Chem., Int. Ed*. **2020**, *59*, 3961-3965.

[19] S. A. Hassanzadeh-Tabrizi, D. Davoodi, A. A. Beykzadeh, S. Salahshour, *Ceram. Int*. **2016**, *42*, 1812-1816.

[20] X. Zou, L. Wang, X. Ai, H. Chen, X. Zou, *Chem. Commun.* **2020**, *56*, 3061-3064.

[21] Y. Yao, Z. Huang, P. Xie, S. D. Lacey, R. J. Jacob, H. Xie, F. Chen, A. Nie, T. Pu, M. Rehwoldt, D. Yu, M. R. Zachariah, C. Wang, R. Shahbazian-Yassar, J. Li, L. Hu, *Science* **2018**, *359*, 1489.

[22] C. H. Choi, J. Shin, L. Eddy, V. Granja, K. M. Wyss, B. Damasceno, H. Guo, G. Gao, Y. Zhao, C. Fred Higgs III, Y. Han, J. M. Tour, *Nat. Chem*. **2024**, *16*, 1831.

[23] D. Portehault, S. Devi, P. Beaunier, C. Gervais, C. Giordano, C. Sanchez, M. Antonietti, *Angew. Chem. Int. Ed*. **2011**, *123*, 3320–3323.

[24] S. Gupta, M. K. Patel, A. Miotello, N. Patel, *Adv. Funct. Mater*. **2020**, *30*, 1906481.

[25] S. Carenco, D. Portehault, C. Boissière, N. Mézailles, C. Sanchez, *Chem. Rev*. **2013**, *113*, 7981–8065.

[26] J. Ma, N. Li, Q. Zhang, X. Zhang, J. Wang, K. Li, X. Hao, J. Yan, *Energy Environ. Sci*. **2018**, *11*, 2833–2838.

[27] Q. Li, X. Zou, X. Ai, , H. Chen, L. Sun, X. Zou, *Adv. Energy Mater.* **2019**, *9*, 1803369.

[28] F. Guo, Y. Wu, H. Chen, Y. Liu, L. Yang, X. Ai, X. Zou. *Energy Environ. Sci*. **2019**, *12*, 684-692.

[29] D. Chen, T. Liu, P. Wang, J. Zhao, C. Zhang, R. Cheng, W. Li, P. Ji, Z. Pu, S. Mu, *ACS Energy Lett*. **2020**, *5*, 2909–2915.

[30] D. Jeon, D. Kim, H. Kim, N. Kim, C. Lee, D. H. Seo, J. Ryu, *Adv. Mater*. **2024**, *36*, 2304468.

[31] Z. Pu, I. S. Amiinu, Z. Kou, W. Li, S. Mu, *Angew. Chem. Int. Ed*. **2017**, *56*, 11559.

[32] Z. Wang, X. Hao, Z. Jiang, X. Sun, D. Xu, J. Wang, H. Zhong, F. Meng, X. Zhang, *J. Am. Chem. Soc*. **2015**, *137*, 15070-15073.

[33] J. Han, H. Wang, Y. Wang, H. Zhang, J. Li, Y. Xia, J. Zhou, Z. Wang, M. Luo, Y. Wang, N. Wang, E. Cortés, Z. Wang, A. Vomiero, Z. Huang, H. Ren, X. Yuan, S. Chen, D. Feng, X. Sun, Y. Liu, H. Liang, *Angew. Chem. Int. Ed*. **2017**, *10*, 788–798.

[34] Y. Tang, M. Gao, C. Liu, S. Li, H. Jiang, Y. Lan, M. Han, S. Yu, *Angew. Chem., Int. Ed*. **2015**, *54*, 12928–12932.

[35] W. Shi, Z. Li, Z. Gong, Z. Liang, H. Liu, Y. Han, H. Niu, B. Song, X. Chi, J. Zhou, H. Wang, B. Xia, Y. Yao, Z. Tian, *Nat. Commun*. **2023**, *14*, 2294.

[36] J. Chen, C. Chen, M. Qin, B. Li, B. Lin, Q. Mao, H. Yang, B. Liu, Y. Wang, *Nat. Commun*. **2022**, *13*, 5382.

[37] Y. Zhang, X. Mu, Z. Liu, H. Zhao, Z. Zhuang, Y. Zhang, S. Mu, S. Liu, D. Wang, Z. Dai. *Nat. Commun*. **2024**, *15*, 10149.

[38] K. Yao, J. Li, A. Ozden, H. Wang, N. Sun, P. Liu, W. Zhong, W. Zhou, J. Zhou, X. Wang, H. Liu, Y. Liu, S. Chen, Y. Hu, Z. Wang, D. Sinton, H. Liang, *Nat. Commun*. **2024**, *15*, 1749.

[39] H. C. Jo, K. M. Kim, H. Cheong, S. H. Lee, S. K. Deb, *Solid St. Lett*. **2005**, *8*, E39-E41.

[40] S. Tominaka, R. Ishibiki, A. Fujino, K. Kawakami, K. Ohara, T. Masuda, I. Matsuda, H. Hosono, *Chem* **2020**, *6*, 406-418.

[41] H. Chen, X. Zou, *Inorg. Chem. Front.* **2020**, *7*, 2248-2264.

[42] Y. Zheng, Y. Jiao, Y. Zhu, L. Li, Y. Han, Y. Chen, A. Du, M. Jaroniec, S. Qiao, *Nat. Commun*. **2014**, *5*, 3783.

[43] J. Gu, S. Liu, W. Ni, W. Ren, S. Haussener, X. Hu, *Nat. Catal*. **2022**, *5*, 268–276.

[44] J. Li, Z. Wang, C. McCallum, Y. Xu, F. Li, Y. Wang, C. M. Gabardo, C. Dinh, T. Zhuang, L. Wang, J. Y. Howe, Y. Ren, E. H. Sargent, D. Sinton, *Nat. Catal*. **2019**, *2,* 1124–1131.

[45] H. Li, H. Li, P. Wei, Y. Wang, Y. Zang, D. Gao, G. Wang, X. Bao, *Energy Environ. Sci*. **2023**, *16*, 1502–1510.

10.1002/anie.202425257

WILEY VCH

Entry for the Table of Contents

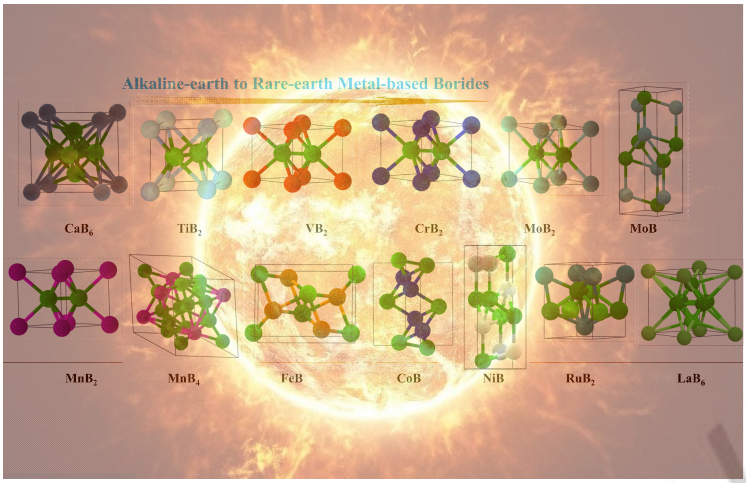

Borides based on alkaline earth to rare-earth metals can be synthesized using the flash Joule heating technique within 60 seconds. The ultrafast synthesis methods confer exceptional physicochemical properties upon these materials, thereby enabling diverse application potentials across various fields.